

See discussions, stats, and author profiles for this publication at: <https://www.researchgate.net/publication/279729730>

In Situ Photocatalytically Heterostructured ZnOAg Nanoparticle Composites as Effective Cathode-Modifying Layers for Air-Processed Polymer Solar Cells

ARTICLE *in* CHEMISTRY - A EUROPEAN JOURNAL · JULY 2015

Impact Factor: 5.73 · DOI: 10.1002/chem.201405073 · Source: PubMed

READS

3

3 AUTHORS, INCLUDING:



Kai Yuan

Bergische Universität Wuppertal

22 PUBLICATIONS 126 CITATIONS

[SEE PROFILE](#)



Lie Chen

Nanchang University

124 PUBLICATIONS 863 CITATIONS

[SEE PROFILE](#)

Synthesis Design

In Situ Photocatalytically Heterostructured ZnO–Ag Nanoparticle Composites as Effective Cathode-Modifying Layers for Air-Processed Polymer Solar Cells

Kai Yuan,^[a] Lie Chen,^[a, b] and Yiwang Chen^{*[a, b]}

Abstract: A heterostructured semiconductor–metal ZnO–Ag nanoparticle (NP) composite was constructed through a straightforward photocatalytic strategy by using UV irradiation of ZnO NPs and an aqueous solution of Ag precursor. The ZnO–Ag NP composites serve as an effective cathode-modifying layer in polymer solar cells (PSCs) with increased short-circuit current density owing to the light-trapping effect, and improved optical and electrical conductivity properties compared with pure ZnO NPs. The Ag NPs, which are photodeposited *in situ* on ZnO NPs, can act as effective antennas for incident light to maximize light harvesting and

minimize radiative decay or nonradiative losses, consequently resulting in the enhanced photogeneration of excitons in PSCs. Systematic photoelectron and -physical investigations confirm that heterostructured ZnO–Ag NPs can significantly improve charge separation, transport, and collection, as well as lower charge recombination at the cathode interface, leading to a 14.0% improvement in air-processed device power conversion efficiency. In addition, this processable, cost-effective, and scalable approach is compatible with roll-to-roll manufacturing of large-scale PSCs.

Introduction

Polymer solar cells (PSCs), based on bulk heterojunction (BHJ) active-layer composites of conjugated polymer donors and fullerene derivative acceptors, are envisioned to be promising candidates for the development of lightweight, flexible, low-cost, portable, and renewable energy sources.^[1] In conventional PSCs, a low work-function metal (such as Al, Ca) is typically used as the top cathode for efficient electron extraction, which, however, is chemically unstable and susceptible to fast corrosion by oxygen and water vapor, making this device configuration not viable for large-scale roll-to-roll processing.^[2] In addition, the transparent indium tin oxide (ITO) conductive anode may be etched easily by a very hygroscopic and corrosive anode buffer layer, such as typical poly(3,4-ethylenedioxythiophene):poly(styrenesulfonate) (PEDOT:PSS), which causes device degradation and dramatically decreases the stability of the device.^[3]

To overcome these challenges, the inverted device geometry, consisting of a BHJ photoactive layer between the ITO cathode modified by metal oxides (such as ZnO, TiO_x) or metal carbonates, which is used to collect electrons, and the air-stable high work-function metal (such as Ag and Au) top anode in combination with an appropriate interfacial layer to collect holes, has been proposed as a more practical architecture for existing roll-to-roll processes and commercialization.^[2–4] Moreover, by reversing the polarity of charge collection, inverted PSCs can also take advantage of the vertical phase separation and concentration gradient in the active layer that favors charge transport and collection, which can significantly improve photovoltaic device performance and natural self-encapsulation because air-stable metals are used as the top electrode.^[3b, 4b] Recently, the power conversion efficiency (PCE) of inverted PSCs has exceeded 9% for single-stack structures and 10% for tandem structures.^[3b, 5] Therefore, the inverted device architecture is a desired configuration for various PSCs.

Among different types of metal oxides as cathode-modifying materials used in inverted PSCs, ZnO has been regarded as a promising candidates due to its high optical transparency, exceptional thermal and chemical stability, environmental friendliness, hole blocking property, and suitable electron selectivity.^[6] Moreover, the solution processability of ZnO nanoparticles (NPs) has been shown through easy processing into thin films by spin coating at room temperature, which is compatible with the large-area roll-to-roll printing process used for PSCs.^[7] Despite such advantages, the relatively low electrical conductivity and inherent limitations in charge transport of solution-processed ZnO NPs is not suffi-

[a] K. Yuan,⁺ Prof. Dr. L. Chen,⁺ Prof. Dr. Y. Chen

College of Chemistry/Institute of Polymers
Nanchang University, 999 Xuefu Avenue
Nanchang 330031 (P.R. China)

[b] Prof. Dr. L. Chen,⁺ Prof. Dr. Y. Chen

Jiangxi Provincial Key Laboratory of New Energy Chemistry
Nanchang University, 999 Xuefu Avenue
Nanchang 330031 (P.R. China)
Fax: (+86) 791-83969561
E-mail: ywchen@ncu.edu.cn

[†] These authors contributed equally to this work.

Supporting information for this article is available on the WWW under
<http://dx.doi.org/10.1002/chem.201405073>.

cient to afford even a reasonable performance.^[8] A high annealing temperature (usually over 200 °C) is thus used to enhance electrical conductivity by removing residual organic compounds and promote crystallization.^[9] However, this procedure is incompatible with flexible substrates and roll-to-roll technology.

Recently, a number of examples have demonstrated that the formation of a semiconductor–metal composite nanostructure can enhance the catalytic, electronic, and optical properties of semiconductor and metal NPs.^[10] In the areas of photocatalysis, solar energy conversion, and photoelectron device, metal NPs are often incorporated into the ZnO-based semiconductor nanostructure (such as Au–ZnO and Ag–ZnO) to improve the separation of the photoinduced charge carriers and charge transfer.^[10d,e,11] Due to the relatively high environmental stability and significantly lower cost than other noble metals, silver is the primary choice among many proposed metals. Although several photo- or chemical-reduction methods have been developed for fabricating ZnO–Ag composite structures, the syntheses of ZnO and Ag NPs are separate in some processes and, therefore, limit electrical conductivity and charge transfer.^[10b,d,e,12]

Herein, to resolve this bottleneck, we present a straightforward photocatalytic approach to produce heterostructured ZnO–Ag NPs with a light-trapping effect and employ them as an effective cathode-modifying layer in PSCs with increased short-circuit current density, owing to improved optical and electrical conductivity properties compared with pure ZnO NPs. The heterostructured ZnO–Ag NPs were constructed through a simple procedure with UV irradiation of ZnO NPs and a solution of Ag precursor, in which the Ag NPs were spontaneously photodeposited *in situ* on ZnO NPs to form a semiconductor–metal hetero-NP upon UV irradiation. This low-cost, scalable approach is compatible with roll-to-roll technology. In addition, silver NPs can act as effective antennas for incident light to maximize light harvesting and minimize radiative decay or nonradiative losses, resulting in the enhanced photogeneration of excitons in PSCs.^[13] Systematic photoelectron and -physical analyses confirm that heterostructured ZnO–Ag NPs can improve charge separation, transport, and collection and decrease charge recombination at the cathode interface. Therefore, heterostructured ZnO–Ag NPs as a cathode-modifying layer promote an air-processed device based on poly[4,8-bis-(2-ethylhexylthiophene-5-yl)benzo[1,2-*b*:4,5-*b*]dithiophene-2,6-diyl]-*alt*-[2-(2-ethylhexanoyl)thieno[3,4-*b*]thiophen-4,6-diyl] (PBDTTT-C-T)^[14] and [6,6]-phenyl C₇₁-butyric acid methyl ester (PC₇₀BM) with an improved PCE (7.48%) compared with that of pure ZnO (6.56%).

Results and Discussion

In a bid to guarantee the controllable deposition of Ag NPs on the ZnO surface, the synthesis of ZnO–Ag NP composites takes advantage of the photoexcitation of ZnO NPs under UV irradiation to produce electrons for the reduction of Ag precursors (AgNO₃) directly on the ZnO surface. The photocatalytic reaction was performed in water. First, the ZnO NPs were syn-

thesized according to a procedure reported previously. AgNO₃ was then introduced into the reaction system by mixing with a dispersion of ZnO NPs in deionized water. In a typical photocatalytic reaction, an aqueous solution containing ZnO NPs and AgNO₃ was irradiated under a UV lamp at $\lambda = 254$ nm for 1 h. The ZnO NPs were photoexcited with UV illumination in the presence of AgNO₃, which reduced the Ag⁺ ions to Ag NPs through electron transfer from the photoexcited ZnO NPs. In this procedure, the Ag NPs tend to form on the surface of the ZnO NPs, as illustrated in Figure 1a. Details of the synthesis of ZnO–Ag NP composites are provided in the Experimental Section.

TEM images of ZnO and ZnO–Ag NPs are shown in Figure S1 in the Supporting Information. The corresponding HR-TEM images of ZnO and ZnO–Ag NPs are presented in Figure 1b and c, respectively. The formation of Ag NPs on ZnO NPs can be clearly observed from the TEM and HR-TEM images thanks to the higher contrast of Ag than that of ZnO. The HR-TEM image of an individual ZnO–Ag NP (Figure 1c) reveals a dimer-type heterostructure of ZnO–Ag NPs (i.e., Ag NP is embedded in the ZnO NP). The HR-TEM image (Figure 1c) shows a distinguished interface and the continuity of lattice fringes between the Ag and ZnO NPs, which confirms the formation of Zn–O...Ag bonds at the interfaces between Ag and ZnO NPs.^[10d] This result is also supported by a comparison of the TEM images of ZnO–Ag NPs, Ag NPs, and ZnO + Ag NPs (mixture of ZnO and Ag NPs), as shown in Figure S1 in the Supporting Information. The ZnO NPs show a uniform lattice structure with an average diameter of about 18 nm and a distinguishable space between adjacent lattice fringes of 0.26 nm, which is ascribed to the 002 lattice plane of ZnO. The Ag NPs have an average diameter of about 7 nm and a lattice fringe of 0.23 nm, which is assigned to the 111 lattice plane of Ag. The inset of Figure 1c shows the energy-dispersive X-ray (EDX) spectrum of the ZnO–Ag NPs. Three elements, Zn, Ag, and O, can be clearly detected, which further confirms the formation of ZnO–Ag NP composites.

A comparison of the steady-state UV/Vis absorption spectra of ZnO, ZnO + Ag, and ZnO–Ag NPs in solution is presented in Figure 2a. After UV irradiation for 1 h, both the absorption of the ZnO NPs and the characteristic surface plasmon resonance (SPR) peak resulting from Ag NPs are observed in the ZnO–Ag sample, but no specific peak for Ag NPs appears for the solution of ZnO NPs. The appearance of two prominent characteristic absorption bands verifies that the as-synthesized ZnO–Ag nanocomposites are composed of ZnO and Ag NPs. After UV irradiation, the solution of a blend of ZnO and AgNO₃ turned dark brown, which also implied the conversion of Ag⁺ ions into Ag NPs (Figure 2a, inset). In contrast to the SPR peak obtained for a mixture of ZnO and Ag NPs of a similar size, ZnO–Ag NPs show a 12 nm redshift of the SPR peak and a broader absorption in the range of $\lambda = 400$ –650 nm. The reason for the broadening and redshift of the SPR peak of the Ag NPs in the ZnO–Ag NP composites is due to strong interfacial coupling between neighboring ZnO and Ag NPs. The lower Fermi energy level and higher work function of ZnO than that of Ag results in electron transfer from Ag to ZnO. It is well-known

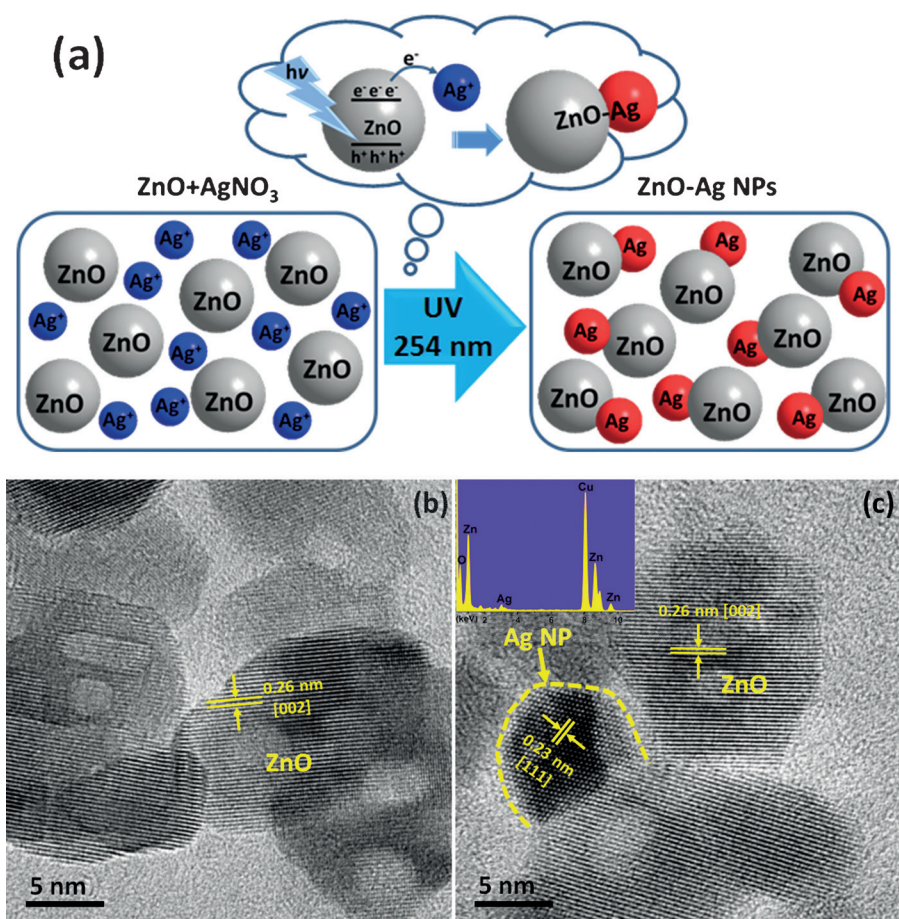


Figure 1. a) The proposed formation mechanism for ZnO–Ag NP composites and a schematic illustration of the ZnO NPs and AgNO₃ blend solution before (left) and after (right) UV irradiation. High-resolution (HR) TEM images of ZnO NPs (b) and ZnO–Ag NPs (c). The parallel lines in yellow show the distinguishable lattice fringes (0.26 and 0.23 nm) of ZnO NPs and Ag NPs, respectively. The inset of c) shows elemental analysis by energy-dispersive X-ray spectroscopy (EDX), which supports the formation of ZnO–Ag NPs.

that the position of the SPR peaks of metal NPs depends on the free electron density of the metal [Eq. (1)]:^[15]

$$\lambda = (4\pi^2 c^2 m_e \epsilon_0 / Ne^2)^{1/2} \quad (1)$$

in which λ is the SPR absorption wavelength, m_e and N are the effective mass and density of free electrons of the metal, respectively, and ϵ_0 is the component of the dielectric permeability of the metal. When the electron density, N , of the metal is decreased, the wavelength (λ) of the SPR absorption increases, which results in a redshift of the absorption. Thus, the redshift in ZnO–Ag is due to decreased electron density of Ag NPs caused by electron transfer from the Ag NPs to ZnO. The XRD patterns of ZnO, ZnO+Ag, and ZnO–Ag nanocomposites are shown in Figure 2b. The (111), (200), and (220) diffraction peaks of face-centered cubic (fcc) Ag (JCPDS file no. 04-0783) and the (100), (002), (101), and (102) peaks of wurtzite ZnO (JCPDS file no. 36-1451) in the XRD patterns of ZnO–Ag nanocomposites are similar to the ZnO+Ag sample; this provides evidence that the ZnO–Ag NPs contain Ag and ZnO NPs.^[10d]

High-resolution X-ray photoelectron spectroscopy (XPS) of ZnO, ZnO+Ag, and ZnO–Ag nanocomposites was carried out to further support the successful preparation of ZnO–Ag NPs. The binding energy peaks in the XPS spectra presented in Figure 2c indicate that ZnO–Ag particles contain Zn, O, and Ag. The peaks located at 367.5 and 373.5 eV of the ZnO–Ag NPs sample are ascribed to the binding energies of Ag 3d_{5/2} and Ag 3d_{3/2}, respectively. Additionally, the binding-energy gap between the Ag 3d_{5/2} and Ag 3d_{3/2} electronic states is 6.0 eV, which is characteristic of metallic Ag, and the same as the Ag 3d peaks of the ZnO+Ag NPs sample.^[16] The XPS data are consistent with the HR-TEM, EDX, XRD, and UV/Vis results. Therefore, UV irradiation of an aqueous solution of ZnO and AgNO₃ blend is capable of producing ZnO–Ag heterostructured NPs. Figure 2d presents the Zn 2p XPS spectra for ITO/ZnO NPs, ITO/ZnO+Ag NPs, and ITO/ZnO–Ag NPs. We found that the Zn 2p peaks were shifted by the presence of Ag NPs in ZnO–Ag relative to ZnO and ZnO+Ag, which supported the proposal that the electronic structure of ZnO in the ZnO–Ag NPs indeed changed. The binding energy of the Zn 2p_{3/2} and Zn 2p_{1/2} electrons in ZnO and ZnO+Ag peaked at 1021.3 and 1044.2 eV, respectively, whereas the binding energies of the Zn 2p_{3/2} and Zn 2p_{1/2} electrons in the ZnO–Ag NPs shifted to 1021.7 and 1044.6 eV, respectively.

The optical properties of ITO/ZnO–Ag are compared with those of bare ITO and ITO/ZnO films. Figure 3a presents the optical transmission spectra in the UV/Vis wavelength range from $\lambda=300$ to 1000 nm. The transmittance of the buffer-layer window plays an important role in determining the amount of light that reaches the photoactive layer and, in turn, the performance of the PSCs.^[17] Bare ITO, ITO/ZnO, and ITO/ZnO–Ag films exhibit optical transmittance values of over 85% in the entire UV/Vis region. The ITO/ZnO–Ag film exhibits a higher transmittance than those of bare ITO and the ITO/ZnO film in the visible range of $\lambda=450$ –590 nm. At $\lambda=500$ nm, the transmittance value of the ITO/ZnO–Ag film is 93.5%, whereas the transmittance values of bare ITO and ITO/ZnO film are 85.8 and 86.3%, respectively. This increase in transmittance is attributed to antireflection caused by the ZnO–Ag NP coatings on

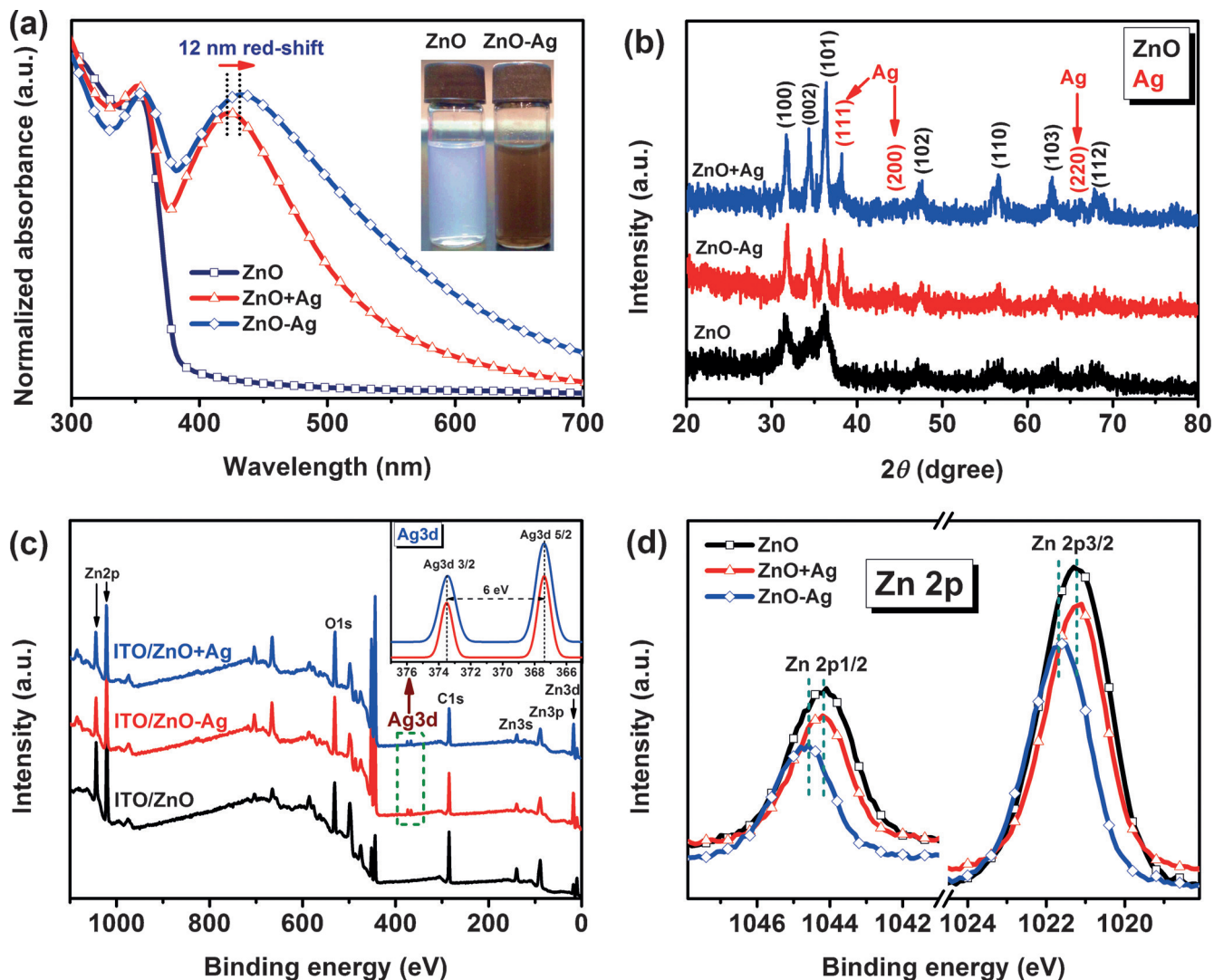


Figure 2. a) A comparison of UV/Vis absorption spectra of ZnO, ZnO + Ag (a mixture of ZnO and Ag NPs), and ZnO–Ag NPs in solution. The inset presents a photograph of solutions of ZnO and ZnO–Ag NPs. b) XRD patterns of ZnO, ZnO + Ag, and ZnO–Ag NPs. c) Survey XPS spectra for ITO/ZnO NPs, ITO/ZnO + Ag NPs, and ITO/ZnO–Ag NPs. The inset presents the Ag 3d peaks of ITO/ZnO + Ag and ITO/ZnO–Ag NPs. d) Zn 2p XPS spectra for ITO/ZnO NPs, ITO/ZnO + Ag NPs, and ITO/ZnO–Ag NPs.

the surface of the ITO substrates. These results suggest that ZnO–Ag is a desirable candidate for solar cell applications.

The potential application of the ZnO–Ag NP composites in photovoltaics was explored by incorporating them in the construction of inverted PSCs. The device configuration is illustrated in Figure 3 b. Two active layers based on P3HT:PC₆₀BM and PBDTTT-C-T:PC₇₀BM blends are employed. Figure 3 c,d presents the current density–voltage (*J*–*V*) curves of inverted PSCs based on P3HT:PC₆₀BM and PBDTTT-C-T:PC₇₀BM with ZnO, ZnO + Ag, and nanostructured ZnO–Ag layer under illumination (AM 1.5G, 100 mW cm⁻²) and in the dark. The photovoltaic performance parameters of eight devices are summarized in Table 1. Figure 4 c shows the *J*–*V* curves of the PSCs based on P3HT:PC₆₀BM under illumination and in the dark. The device with the ZnO layer gives a PCE of 3.56% with a *J*_{sc} of 9.10 mA cm⁻², a *V*_{oc} of 0.61 V, and a fill-factor (FF) of 64.1%. The device with ZnO + Ag shows a slight change in PCE (3.75%)

with a *J*_{sc} of 9.51 mA cm⁻², a *V*_{oc} of 0.61 V, and a FF of 64.7%. In contrast, the PCE of the device with the nanostructured ZnO–Ag layer is clearly improved to 4.02% due to the distinctly enhanced *J*_{sc} (10.08 mA cm⁻²) and slightly increased FF (65.3%). A similar tendency can be detected for the devices based on PBDTTT-C-T:PC₇₀BM (Figure 3 d). The device with ZnO layer has a *J*_{sc} of 14.73 mA cm⁻², a *V*_{oc} of 0.76 V, a FF of 58.6%, and a PCE of 6.56%. The device with ZnO + Ag has a *J*_{sc} of 15.36 mA cm⁻², a *V*_{oc} of 0.76 V, and a FF of 58.3% to yield a PCE of 6.81%. As expected, the device with the nanostructured ZnO–Ag layer displays a remarkably enhanced PCE of 7.48%, together with a *J*_{sc} of 16.49 mA cm⁻², a *V*_{oc} of 0.76 V, and a FF of 59.7%. The higher PCE of the device with ZnO–Ag than that with ZnO + Ag is due to strong interfacial coupling and the synergistic effect of ZnO and Ag in the ZnO–Ag NP composites. That PCE greatly improved by 14.0% is mainly attributed to the significant increase in *J*_{sc}. In addition, the *V*_{oc} remained almost un-

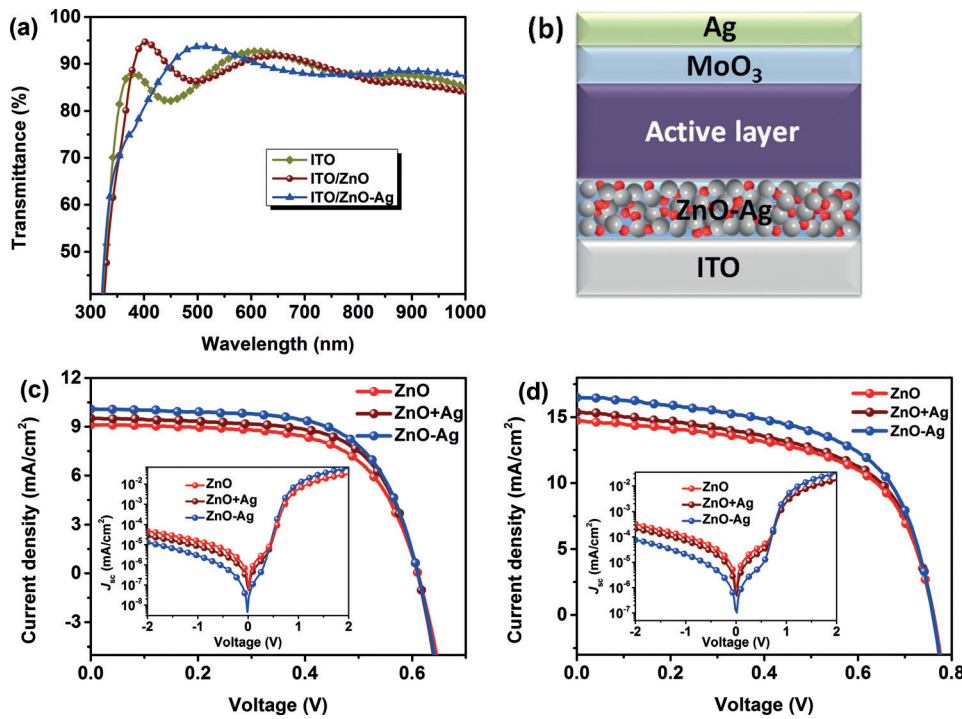


Figure 3. a) Transmittance spectra of ITO glass, ITO glass/ZnO, and ITO glass/ZnO–Ag electrodes. b) Schematic illustration of the device configuration. d) J–V characteristics of devices with ZnO, ZnO+Ag, and ZnO–Ag layers based on c) poly(3-hexylthiophene) (P3HT):[6,6]-phenyl-C₆₁ butyric acid methyl ester (PC₆₀BM) and d) PBDTTT-C-T:PC₇₀BM under AM1.5 illumination (at 100 mW cm⁻²) and dark (insets of c and d).

Table 1. Photovoltaic properties of devices based on ZnO, ZnO+Ag, and ZnO–Ag NPs under AM 1.5G illumination (100 mW cm ⁻²), and the corresponding electron mobilities of the devices. ^[a]							
Device	J_{sc} [mA cm ⁻²]	V_{oc} [V]	FF [%]	PCE [%]	R_s ^[b] [Ω cm ⁻²]	R_{sh} ^[b] [Ω cm ⁻²]	μ_e ^[c] [m ² V ⁻¹ s ⁻¹]
ZnO/P3HT:PC ₆₀ BM	9.10	0.61	64.1	3.56	2.4	1276.1	6.73×10^{-5}
ZnO+Ag/P3HT:PC ₆₀ BM	9.51	0.61	64.7	3.75	2.3	1369.5	7.61×10^{-5}
ZnO–Ag/P3HT:PC ₆₀ BM	10.08	0.61	65.3	4.02	1.8	1860.7	9.67×10^{-5}
ZnO/PBDTTT-C-T:PC ₇₀ BM	14.73	0.76	58.6	6.56	3.8	839.3	1.12×10^{-4}
ZnO+Ag/PBDTTT-C-T:PC ₇₀ BM	15.36	0.76	58.3	6.81	3.3	843.7	1.56×10^{-4}
ZnO–Ag/PBDTTT-C-T:PC ₇₀ BM	16.49	0.76	59.7	7.48	1.7	878.8	2.67×10^{-4}

[a] J_{sc} =short-circuit current density, V_{oc} =open-circuit voltage, FF=fill factor, R_s =series resistance, R_{sh} =shunt resistance, μ_e =electron mobility. [b] R_s and R_{sh} were deduced from the J–V curves. [c] Electron-only device configuration: ITO/ZnO or ZnO–Ag//PBDTTT-C-T:PC₇₀BM/Al.

changed; this was ascribed to negligible changes in the work function between ZnO and the ZnO–Ag layer, which was supported by the UV photoelectron spectroscopy (UPS) and Kelvin measurements, as shown in Figures S2 and S3 in the Supporting Information.

To find the intrinsic reasons behind the J_{sc} enhancement of the PSCs, AFM images were employed to investigate the surface morphology difference in the ZnO and ZnO–Ag layers before and after coating with PBDTTT-C-T:PC₇₀BM active layers (see Figure S4 in the Supporting Information). Based on the AFM results, the root-mean-square (RMS) roughness values for ZnO and ZnO–Ag were found to be 3.68 and 3.53 nm, respectively. After coating with PBDTTT-C-T:PC₇₀BM active layers, the

increased absorption between $\lambda=350$ and 700 nm compared to that on ZnO layer (Figure 4c). These results suggest that the enhancement in J_{sc} can be ascribed to the plasmonic effect of the ZnO–Ag NPs that can regulate the optical properties of the photoactive layer to obtain the optimal overall absorption enhancement, and achieve higher exciton generation of the device and contribute to the improved EQE and light harvesting.^[10b,c, 13a, 20]

The J_{sc} value is directly related to the EQE, which is predominantly affected by the overall carrier dynamics, including the product of light absorption, exciton diffusion efficiency, charge-transfer efficiency, and charge-collection efficiency.^[21] To gain more insight into the origin of the performance enhance-

RMS values for ZnO and ZnO–Ag were reduced to 1.83 and 1.72 nm, respectively. This inconspicuous difference in roughness of ZnO, ZnO–Ag, and the active layer should not affect the device performance.^[18]

Because the morphology difference between the ZnO and ZnO–Ag layers before and after being covered with active layers is not the primary reason for the enhancement in J_{sc} , we measured and compared the external quantum efficiency (EQE) and total absorption efficiency (TAE) spectra of the devices based on PBDTTT-C-T:PC₇₀BM. The TAE can be derived from a reflection measurement as $TAE=1-R$, in which R is the measured reflection from the device, as shown in Figure S5 in the Supporting Information.^[19]

Figure 4a plots the measured EQEs and TAEs for the PSCs fabricated with the ZnO and ZnO–Ag layer, and relative TAE and EQE enhancements are presented in Figure 4b. The device with the ZnO–Ag layer shows an enhancement over a wide range from $\lambda=350$ to 720 nm in both EQE and TAE compared with the device with the ZnO layer. The EQE and TAE enhancement spectra of the devices based on P3HT:PC₆₀BM show a similar tendency, as presented in Figure S6 in the Supporting Information. In addition, the steady-state UV/Vis absorption spectra of the PBDTTT-C-T:PC₇₀BM active layer on ZnO–Ag layer exhibits an in-

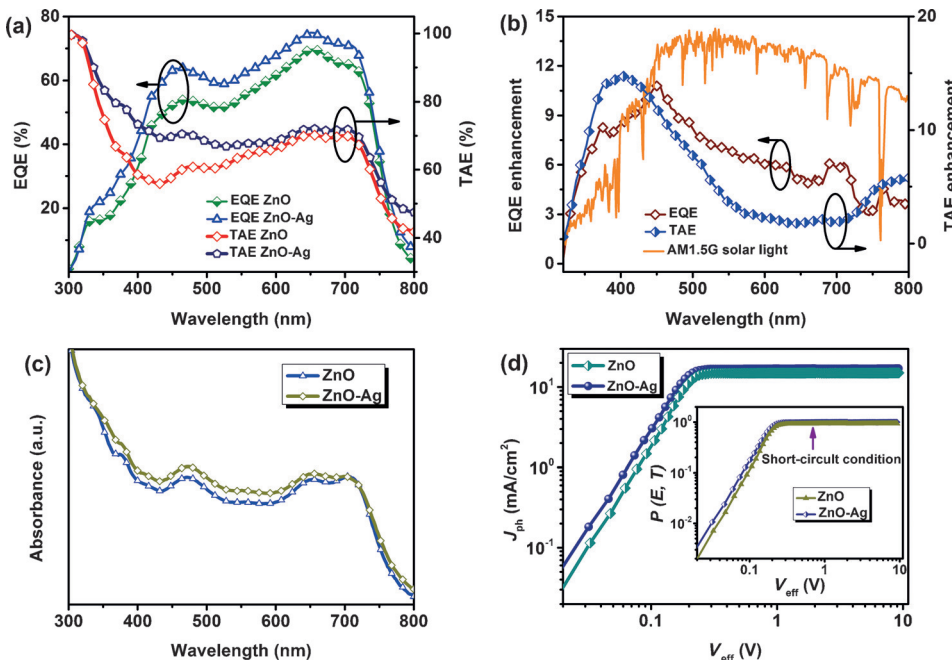


Figure 4. a) External quantum efficiency (EQE) and total absorption efficiency (TAE) values of devices based on PBDTTT-C-T:PC₇₀BM with ZnO and ZnO–Ag NPs. b) EQE and TAE enhancements of the ZnO–Ag NP based device over the ZnO-based device, as well as the photon density of AM 1.5G solar light. c) Optical absorption spectra of the PBDTTT-C-T:PC₇₀BM active layer coated on ZnO and ZnO–Ag NPs with quartz substrates. d) Photocurrent density (J_{ph}) versus effective voltage (V_{eff}) characteristics of ZnO- and ZnO–Ag NP based devices. Inset: Exciton dissociation probability, $P(E,T)$, as a function of V_{eff} for ZnO- and ZnO–Ag NP based devices.

ment, light absorption, and the exciton dissociation process, we determined the saturation current density (J_{sat}), the maximum photoinduced carriers generation rate (G_{max}), and the charge dissociation probabilities $P(E,T)$ of the devices based on PBDTTT-C-T:PC₇₀BM with ZnO and ZnO–Ag NPs. Figure 4d presents photocurrent density (J_{ph}) versus effective voltage (V_{eff}) curves for the devices based on PBDTTT-C-T:PC₇₀BM with ZnO and ZnO–Ag NPs. Here, J_{ph} is defined as $J_{ph} = J_L - J_D$, in which J_L and J_D are the current densities under illumination and in the dark, respectively. The V_{eff} value is determined as $V_{eff} = V_0 - V_a$, in which V_0 and V_a are the voltage when J_{ph} equals zero and the applied bias voltage, respectively.^[22] If we assume that all photogenerated excitons are dissociated into free charge carriers and collected by electrodes at a high V_{eff} (i.e., $V_{eff} = 2$ V or above), the J_{sat} value will be limited only by the total amount of absorbed incident photons. Therefore, the G_{max} value can be calculated by the formula $J_{sat} = qG_{max}L$, in which q is the elementary charge and L is the thickness of the active layer.^[22,23] The J_{sat} values of the devices with ZnO and the ZnO–Ag NPs layer are 15.03 ($G_{max} = 9.38 \times 10^{27} \text{ m}^{-3} \text{ s}^{-1}$) and 16.97 mA cm⁻² ($G_{max} = 1.06 \times 10^{28} \text{ m}^{-3} \text{ s}^{-1}$), respectively. The J_{ph} of the devices can be written as $J_{ph} = qP(E,T)G_{max}L$; therefore, the $P(E,T)$ can be calculated by normalizing J_{ph} with $J_{sat}(J_{ph}/J_{sat})$.^[22–24] The $P(E,T)$ value of the device with ZnO–Ag increased to 93.6% from 88.3% for the device with ZnO. These findings show that ZnO–Ag can facilitate charge dissociation in the devices, and consequently lead to improved performance.

In addition to the light-harvesting capability and exciton dissociation, the charge collection efficiency was investigated by

means of conductive atomic force microscopy (C-AFM) and space charge limited current (SCLC) measurements were used to characterize charge carrier transport along the vertical direction. The C-AFM current maps of the ZnO and ZnO–Ag NP layers are presented in Figure 5a and b. The RMS current values of the ZnO and ZnO–Ag NP layers are 7.3 and 25.5 pA, respectively. These qualitative investigations indicate that the electronic conductivity of the ZnO–Ag NP layer is much higher than that of the ZnO layer. The improved electronic conductivity of the ZnO–Ag NP layer was also supported by high-resolution XPS spectra of Zn 2p and O 1s (Figure 2d and Figure S7 in the Supporting Information). Moreover, the high binding energy at 531.6 eV, which is associated with oxygen deficiency, decreases from 58.5% in ZnO to

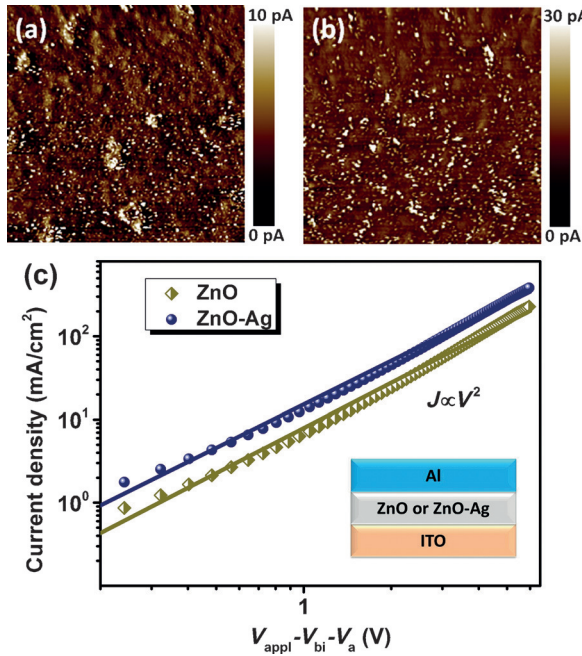


Figure 5. Corresponding current maps ($5 \mu\text{m} \times 5 \mu\text{m}$) of ZnO (a) and ZnO–Ag NP (b) films based on C-AFM measurements. c) J – V curves of the electron-only devices with ZnO and ZnO–Ag NP films. Inset: Configuration of the electron-only devices.

51.3% in ZnO–Ag NPs. The significant reduction in oxygen deficiency will be beneficial for higher electron conductivity.^[2a,6c] This high electronic conductivity will facilitate electron trans-

port from the active layer to the corresponding electrode, resulting in improved charge collection efficiency.^[25]

The *J-V* curves and device configuration of the electron-only device based on ZnO and ZnO–Ag NPs are presented in Figure 5c. The SCLC electron mobilities of ZnO and ZnO–Ag NPs are 2.97×10^{-4} and $5.86 \times 10^{-4} \text{ m}^2 \text{ V}^{-1} \text{ s}^{-1}$, respectively. The increased electron mobility of ZnO–Ag is in good agreement with the C-AFM results. The electron mobilities of the P3HT:PC₆₀BM and PBDTTT-C-T:PC₇₀BM active layers with ZnO, ZnO+Ag, and ZnO–Ag NPs are illustrated in Figure S8 in the Supporting Information and summarized in Table 1. The data show that active layers with ZnO–Ag have higher electron mobilities than those with ZnO and ZnO+Ag. Higher electron mobilities lead to reduced series resistances (Table 1) and better rectification ratios (lower leakage current; insets of Figure 3c and d). Therefore, the incorporation of ZnO–Ag into the PSCs can facilitate charge dissociation and transport, reduce bimolecular recombination and the loss of charge carriers, as well as increase charge collection efficiency.

Conclusion

Heterostructured semiconductor–metal ZnO–Ag NP composites were successfully constructed through a straightforward photocatalytic strategy. PSCs with improved efficiency were demonstrated by employing ZnO–Ag NPs as the cathode-modifying layer due to the light-trapping effect and improved optical and electrical conductivity properties compared with those of pure ZnO NPs. Systematic photoelectron and -physical investigations confirmed that heterostructured ZnO–Ag NP maximized light harvesting and minimized radiative decay or nonradiative losses, which resulted in enhanced photogeneration of excitons; significantly improved charge separation, transport, and collection; and lowered charge recombination probability at the cathode interface. Therefore, the values of J_{sc} and PCE remarkably improved in the air-processed device, which suggested that the solution processable, low-cost, and scalable ZnO–Ag NPs were promising candidates for the development of high-performance roll-to-roll manufactured PSCs.

Experimental Section

Preparation of ZnO NPs

ZnO NPs were synthesized according to procedures reported previously.^[26] Typically, Zn(CH₃COO)₂·2H₂O (2.95 g, 13.4 mmol) was dissolved in methanol (125 mL) with stirring at 60 °C. Then, a solution of KOH (1.48 g, 23 mmol) in methanol (65 mL) was added dropwise to the solution of Zn(CH₃COO)₂·2H₂O over a period of 10 min under vigorous stirring. The mixture was kept at 60 °C for 3 h under stirring. After cooling to room temperature, the resulting turbid precipitate was collected by centrifugation and washed with methanol several times. The final product was redispersed in deionized water to form a slightly translucent dispersion of ZnO NPs with a concentration of 6 mg mL⁻¹ through sonication.

Photocatalytic synthesis of ZnO–Ag nanocomposites

The solution of a mixture of ZnO NPs and AgNO₃ (10:1, w/w) in deionized water was prepared by adding AgNO₃ (3 mg) to a solution of ZnO NPs (5 mL, 6 mg mL⁻¹). The blend solution was placed in a UV quartz cuvette and sealed by a Teflon-faced rubber cap and the mixture was subsequently deaerated with nitrogen for 15 min. Photochemical reduction was carried out by exposing the solution to UV light ($\lambda = 254 \text{ nm}$, with 6 W UV lamp) for 1 h. The quartz cuvette was positioned 5 cm from the light source. After UV irradiation, the dark-brown nanocomposites were collected by centrifugation and washed with deionized water several times. The final product was redispersed in deionized water for device fabrication.

Device fabrication

The ITO-coated glass substrates (10 Ω/square) were cleaned with detergent, deionized water, acetone, and isopropanol under ultrasonication for 15 min each, and then dried under a nitrogen flow followed by O₂ plasma treatment for 10 min. Subsequently, a thin cathode-modifying layer (ZnO, ZnO+Ag, or ZnO–Ag NPs) was spin-coated onto the precleaned ITO-coated glass substrate at 2000 rpm for 1 min. After spin-coating, the substrates were annealed at 150 °C for 10 min to remove water. After annealing, the solutions of the photoactive layer, P3HT:PC₆₀BM or PBDTTT-C-T:PC₇₀BM, with 3% volume ratio of 1,8-diiodooctane additive were spin-coated on the films. After drying of the photoactive layer, a thin (ca. 6 nm) interfacial layer of MoO₃ and a 100 nm thick Ag top electrode were sequentially thermally deposited on top of the photoactive layer to complete the device with an active area of 0.04 cm² controlled by a shadow mask. The final device configurations were glass/ITO/cathode-modifying layer/active layer/MoO₃/Ag.

Characterization

The nanomorphology of ZnO and ZnO–Ag NPs was characterized by field-emission HR-TEM (JEOL, JEM-2100F) with EDX. The HR-TEM samples were prepared by drop-casting solutions of ZnO and ZnO–Ag NPs onto carbon-coated copper grids. The optical characteristics measurements of the samples, including absorption, transmittance, and reflectance spectra, were carried out by using UV/Vis/near-IR spectroscopy (Lambda 750, PerkinElmer). The XRD results for ZnO, ZnO+Ag, and ZnO–Ag NPs were recorded by means of a Bruker D8 Focus X-ray diffractometer with a copper target ($\lambda = 1.54 \text{ \AA}$). The topography of the ZnO and ZnO–Ag NP layers before and after spin-coating with the PBDTTT-C-T:PC₇₀BM active layer was investigated by AFM (Digital Instrumental Nanoscope 31). The current maps of the ZnO and ZnO–Ag NP films were measured by C-AFM. The XPS spectra were collected by using the Kratos AXIS Ultra XPS system. The UPS spectra were recorded by using an AXIS-ULTRA DLD spectrometer (Kratos Analytical Ltd). Photovoltaic performances of the devices were measured under simulated AM 1.5G irradiation (100 mW cm⁻², Abet Solar Simulator Sun2000) and in the dark. The *J-V* curves were collected by using a Keithley 2400 Source Meter. The EQE measurements were achieved by employing the QE system (Oriel Cornerstone 260 1/4 m monochromator equipped with Oriel 70613NS QTH lamp) under monochromatic illumination.

